Magnetic Field Fingerprinting of Integrated-Circuit Activity with a Quantum Diamond Microscope

Matthew J. Turner,[1,2] Nicholas Langellier⬤,[1,3] Rachel Bainbridge,[4] Dan Walters,[4] Srujan Meesala,[1,†]
Thomas M. Babinec⬤,[5] Pauli Kehayias,[6] Amir Yacoby,[1,5] Evelyn Hu,[5] Marko Lončar,[5]
Ronald L. Walsworth⬤,[1,2,3,7,8,9] and Edlyn V. Levine⬤[1,4,*]

[1]*Department of Physics, Harvard University, Cambridge, Massachusetts 02138, USA*

[2]*Center for Brain Science, Harvard University, Cambridge, Massachusetts 02138, USA*

[3]*Center for Astrophysics | Harvard & Smithsonian, 60 Garden Street, Cambridge, Massachusetts 02138, USA*

[4]*The MITRE Corporation, Bedford, Massachusetts 01730, USA*

[5]*John A. Paulson School of Engineering and Applied Sciences, Harvard University, Cambridge,
Massachusetts 02138, USA*

[6]*Sandia National Laboratories, Albuquerque, New Mexico 87123, USA*

[7]*Department of Physics, University of Maryland, College Park, Maryland 20742, USA*

[8]*Department of Electrical and Computer Engineering, University of Maryland, College Park,
Maryland 20742, USA*

[9]*Quantum Technology Center, University of Maryland, College Park, Maryland 20742, USA*

Current density distributions in active integrated circuits result in patterns of magnetic fields that contain structural and functional information about the integrated circuit. Magnetic fields pass through standard materials used by the semiconductor industry and provide a powerful means to fingerprint integrated-circuit activity for security and failure analysis applications. Here, we demonstrate high spatial resolution, wide field-of-view, vector magnetic field imaging of static magnetic field emanations from an integrated circuit in different active states using a quantum diamond microscope (QDM). The QDM employs a dense layer of fluorescent nitrogen-vacancy (N-*V*) quantum defects near the surface of a transparent diamond substrate placed on the integrated circuit to image magnetic fields. We show that QDM imaging achieves a resolution of approximately $10\,\mu$m simultaneously for all three vector magnetic field components over the 3.7×3.7 mm^2 field of view of the diamond. We study activity arising from spatially dependent current flow in both intact and decapsulated field-programmable gate arrays, and find that QDM images can determine preprogrammed integrated-circuit active states with high fidelity using machine learning classification methods.

I. INTRODUCTION

Securing integrated circuits against manufacturing flaws, hardware attacks, and software attacks is of vital importance to the semiconductor industry [1]. Hardware attacks often modify the physical layout of an integrated circuit, thereby changing its function. This type of attack can occur at any stage of the globalized semiconductor supply chain, and can range from insertion of malicious Trojan circuitry during the design and fabrication stages [2], to modification or counterfeiting during the packaging and distribution stages [3]. Horizontal integration of the industry has led to contracting of integrated-circuit fabrication, packaging, and testing to offshore facilities, resulting in a reduction of secure oversight and quality control [4]. Additional growth of the secondhand electronics market has led to a drastic increase in counterfeit integrated circuits [5]. Detection of integrated-circuit tampering or counterfeiting has consequently become essential to ensure hardware can be trusted. Similar issues affect quality control of unintended manufacturing flaws.

Magnetic field emanations from integrated circuits afford a powerful means for nondestructive physical testing. Magnetic fields are generated by current densities in integrated circuits resulting from power and clock distribution networks, input and output lines, word and bit lines, and switching transistors. These currents are present in

*edlynlevine@fas.harvard.edu

†Present address: Thomas J. Watson, Sr. Laboratory of Applied Physics, California Institute of Technology, Pasadena, California 91125, USA.

014097-1

all operating logic and memory chips and can be leveraged for studying the operational behavior of an integrated circuit during task execution. In general, the resulting integrated-circuit magnetic fields pass through many standard integrated circuit materials, and will vary spatially and temporally in ways that correlate with both integrated-circuit architecture and operational state. Thus, combined high-resolution and wide-field-of-view mapping of magnetic fields may yield simultaneous structural and functional information, and may be suitable for identification of malicious circuitry or Trojans [6,7], counterfeit detection [8], fault detection [9–11], and manufacturing flaws [12]. However, leveraging magnetic field emanations is challenging due to the tremendous complexity of circuits integrating billions of transistors of minimum feature sizes down to tens of nanometers, with interconnects distributed across multiple levels of metallization [13]. Multilayered metal interconnects and three-dimensional stacking give rise to complex magnetic field patterns that are difficult to invert, and large standoff distances of magnetometers reduce amplitudes of magnetic fields and spatial resolution [14].

In this paper, we demonstrate how these challenges can be approached using a quantum diamond microscope (QDM) [15–17] augmented with machine learning classification techniques. With the QDM, we perform simultaneous wide field-of-view, high spatial resolution, vector magnetic field imaging of an operational field-programmable gate array (FPGA). FPGAs are configurable integrated circuits that are commonly used for diverse electronics applications. Systematic and controlled variation of the circuit activity in the FPGA generates complex magnetic field patterns, which we image with the QDM. The QDM employs a dense surface layer of fluorescent nitrogen-vacancy (N-V) quantum defects in a macroscopic diamond substrate placed on the integrated circuit under ambient conditions. The electronic spins associated with N-V defects have well-established sensitivity to magnetic fields [18–20].

We use the QDM to image magnetic fields from both decapsulated (decapped) and through-package (intact) FPGAs under operational conditions using continuous-wave (CW) optically detected magnetic resonance (ODMR) N-V spectroscopy. For the decapped FPGA, our measurements yield magnetic field maps that are distinguishable between operational states over approximately a 4×4 mm^2 field of view with a 20 nT noise floor, and a magnetic field spatial resolution of approximately 10 μm, limited by the thickness of the N-V surface layer in the diamond and the distance to the nearest metal layer. For the intact FPGA, the QDM measurements provide magnetic field maps with a similar field of view, 2 nT noise floor, and a magnetic field spatial resolution of approximately 500 μm, limited by the standoff distance between the N-V layer and the FPGA current sources. In particular, we find that operational states of the intact FPGA

are distinguishable in the QDM images, even with the diminished magnetic field amplitude and spatial resolution that arise from the large standoff between the diamond and the integrated circuit die. We use machine learning methods to demonstrate FPGA operational state classification via magnetic field pattern correlation for both decapped and intact FPGA QDM images. This result provides an initial demonstration of functional integrated-circuit characterization via magnetic field fingerprinting. Future work is required to determine whether and how this approach will be useful in areas such as integrated-circuit security and failure analysis.

To date, the QDM's unique combination of magnetic field sensitivity, spatial resolution, field of view, and ease of use has allowed it to be used to measure microscopic current and magnetization distributions from a wide variety of sources in both the physical and life sciences [21–28]. Complementary to scanning techniques for characterizing integrated-circuit magnetic field emanations, which include wire loops [29], probe antennas [30], magnetic force microscopy [11], superconducting quantum interference device magnetometers [7], and vapor cell magnetometers [31], the QDM employs a nonscanning imaging modality [15] that provides simultaneous high-resolution (micron-scale) and wide-field (millimeter-scale) vector magnetic imaging, while operating under ambient conditions. This capability allows for monitoring of transient behavior over sequential measurements of a magnetic field, providing a means to study correlations in signal patterns that can evolve more quickly than a single-sensor scan time. In addition, the QDM's simultaneous magnetic imaging modality is not subject to the reconstruction errors and drift that can arise from a scanned probe. With these distinctive advantages, the QDM technique is a promising approach for nondestructive physical testing of integrated circuits.

II. EXPERIMENTAL DESIGN

A. QDM experimental setup

A schematic of the QDM is shown in Fig. 1(a). The magnetic field sensor consists of a $4 \times 4 \times 0.5$ mm^3 diamond substrate with a 13 μm surface layer of N-V centers. The diamond is placed directly on the integrated circuit with the N-V layer in contact with the integrated-circuit surface. The diamond is grown by Element Six Limited to have an isotopically pure N-V layer consisting of [^{12}C] $\sim$ 99.999%, [^{14}N] $\sim$ 27 ppm, and [N-V^-] $\sim$ 2 ppm. Light from a 532 nm, CW laser (Lighthouse Photonics Sprout-H-10W) optically addresses the N-V layer with a beam power of about 500 mW uniformly distributed over the 4×4 mm^2 N-V layer. A flat-top beam shaping element (Eksma Optics GTH-5-250-4-VIS) and a cylindrical lens (Thorlabs LJ1558RM-A) create a rectangular beam profile (6×6 mm^2) incident on the top face of the diamond
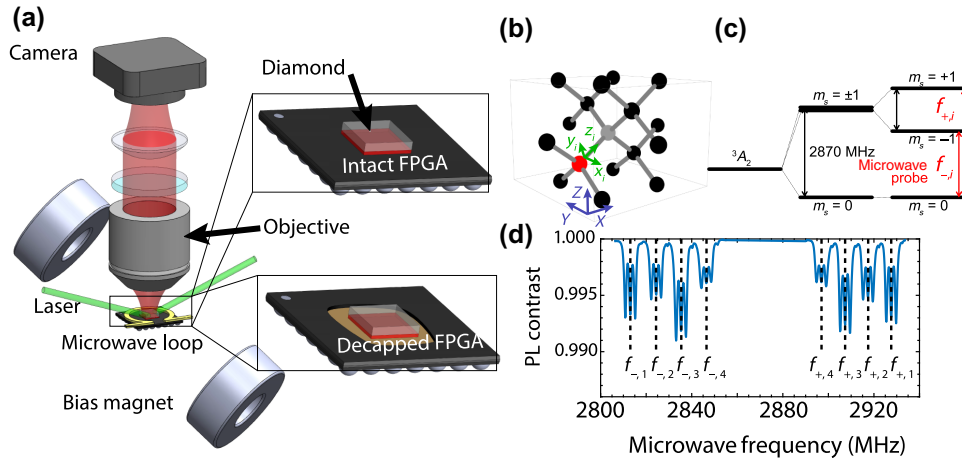
FIG. 1. (a) Schematic of the QDM experimental setup with insets showing the diamond in contact with intact and decapsulated FPGAs. The diamond is positioned such that the N-V layer is in direct contact with the FPGA, as indicated by the red layer in the insets. (b) Diamond crystal lattice with the nitrogen (red) vacancy (grey) defect. Lab frame coordinates (X, Y, Z) and N-V frame coordinates for a single defect (x, y, z) are shown. (c) The ground state energy level diagram for a N-V with fine structure and Zeeman splitting. (d) Example ODMR spectral data for an applied bias field of $(B_X, B_Y, B_Z) = (2.0\ 1.6\ 0.7)$ mT, showing the measured N-V fluorescence contrast, i.e., photoluminescence (PL) contrast, and resonant microwave frequencies of $f_{\pm,i}$ with $i = 1, 2, 3, 4$ indicating each of the four N-V axes. Hyperfine interactions between the N-V^- electrons and the spin-1 ^{14}N nucleus result in the splitting of each N-V resonance into three lines.

at a sufficiently shallow angle of incidence $(4°)$ relative to the top diamond surface to illuminate the entire N-V layer. N-V fluorescence is collected with a low magnification objective (Olympus UPlanFL N 4x 0.13 NA) to interrogate a large field of view of about 3.7×3.7 mm^2. The fluorescence is filtered with a 633 nm longpass filter (Semrock LP02-633RU-25) and imaged onto a CMOS camera (Basler acA1920-155um). Resulting CW ODMR data is transferred to a computer where it is processed and analyzed with custom software utilizing LabVIEW and MATLAB$^{®}$.

A pair of 5 cm diameter SmCo permanent magnets (Super Magnet Man) is placed on opposing sides of the diamond to apply a uniform bias magnetic field (bias field) of $\mathbf{B}_0 = (B_X, B_Y, B_Z) = (2.0, 1.6, 0.7)$ mT to separate the resonances of the different N-V axes [see Fig. 1(d)]. The laboratory frame Cartesian coordinates are X, Y, Z with the X-Y plane defined as the surface of the diamond in Fig. 1(b). The bias field $\mathbf{B}_0$ induces a $\pm g_e\mu_B\mathbf{B}_0 \cdot \mathbf{n}$ Zeeman splitting of the spin triplet N-V $m = 1$ and $m = -1$ ground states along each of four tetrahedrally defined N-V symmetry axes, $\mathbf{n}$, with Landé g-factor g_e, and Bohr magneton μ_B. The hyperfine interaction between the N-V and the ^{14}N isotope nuclear spin $(I = 1)$ results in an additional triplet level splitting. The four symmetry axes of the N-V, shown in Fig. 1(b), are leveraged for vector magnetic field imaging using $\mathbf{B}_0$ projection onto all four N-V axes [32]. The ground state energy level diagram of a single N-V axis is depicted in Fig. 1(c), neglecting the hyperfine structure.

A 6 mm diameter copper wire loop made from 320 μm diameter magnet wire delivers 1 W of gigahertz-frequency

microwave fields (TPI-1001-B and amplified with a Mini-Circuits ZHL-16W-43S+ amplifier) to drive the N-V electronic spin transitions, $m_s = 0 \leftrightarrow -1$ or $m_s = 0 \leftrightarrow +1$, denoted by $f_{-,i}$ and $f_{+,i}$, respectively; see Figs. 1(a) and 1(c). The microwave power chosen is sufficiently low to not effect the observed normal function of the integrated circuit. The microwave field is modulated on and off through the use of a solid-state switch (ZASWA-2-50DRA+) controlled by a DAQ (NI-USB 6259) and synchronized with the frame acquisition of the camera to correct for laser intensity fluctuations and drift.

The intensity of optically induced N-V fluorescence decreases for microwave fields on resonance with one of the spin transition energies. This decrease results from the $m = \pm 1$ spin selectivity of the nonoptical, intersystem crossing (ISC) mediated decay pathway for optically excited N-Vs [33]. The resonance frequencies between N-V ground-state sublevels are determined from the ground-state Hamiltonian

$$H/h = [D(T) + M_z]S_z^2 + \gamma(B_x S_x + B_y S_y + B_z S_z)$$
$$+ M_x(S_y^2 - S_x^2) + M_y(S_x S_y + S_y S_x) \quad (1)$$

for the projection of $\mathbf{B}_0$ along a single N-V axis, where h is Planck's constant, $D(T) \approx 2870$ MHz is the temperature dependent zero-field splitting, T is the temperature, the S_k are the dimensionless spin-1 Pauli operators, $\gamma = 2.803 \times 10^4$ MHz/T is the N-V gyromagnetic ratio, the B_k are the components of $\mathbf{B}_0$ in the N-V frame, and the M_k are crystal stress terms [34]. Electric field terms

contribute minimally and are neglected [35–37]. Cartesian coordinates $k = x, y, z$ are defined in the N-*V* frame with z along the selected N-*V* axis; see Fig. 1(b). The contribution of the hyperfine interaction between the N-*V* and ^{14}N nuclear spin is treated as a constant, 2.158 MHz energy level splitting and is not shown explicitly in Eq. (1). Sweeping the frequency of the applied microwave fields across the range of resonant frequencies and collecting the N-*V* fluorescence results in an ODMR spectrum. Figure 1(d) depicts the resulting ODMR measurements for a bias field alignment where each N-*V* axis experiences a different projection of the bias magnetic field.

Continuous-wave ODMR is used to image static FPGA magnetic fields. CW ODMR leverages continuous application of the laser and microwave field. This approach yields wide field-of-view images with high spatial resolution and good magnetic field sensitivity, while minimally perturbing the sample under study [15,16]. A diamond with sufficiently low M_z inhomogeneity across the field of view is used to minimize degradation of performance [34]. Further suppression of strain contributions is achieved with application of the static bias field, $\mathbf{B}_0$. Thus, the M_x and M_y terms in Eq. (1) are negligible [34,38]. The ground state Hamiltonian along a single N-*V* axis reduces to

$$H/h \approx [D(T) + M_z]S_z^2 + \gamma B_z S_z + \gamma B_x S_x + \gamma B_y S_y, \quad (2)$$

and is used to determine the CW ODMR resonance frequencies for each pixel in a QDM image, and thereby to determine the magnetic field image from the sample FPGA.

B. Integrated-circuit preparation, control, and layout

The Xilinx 7-series Artix FPGA (XC7A100T-1CSG3 24C) shown in Figs. 2(a) and 2(b) is selected for this study owing to its versatility, general availability, and affordability. This FPGA is a 15×15 mm^2 wirebonded chip, fabricated in the TSMC 28 nm technology node, which has an approximately 6.5×10 mm^2 silicon die with eight clock regions. Digilent Nexys A7 development boards are used to operate and configure the Artix-7 FPGA. Two chips are used: one intact Artix 7 and decapsulated(decapped) Artix 7 that is prepared using a Nisene JetEtch Pro CuProtect decapsulator.

The large current draw and controllable location and size of ring oscillators make them ideal functional units for this study [39,40]. Patterns of ring oscillators are implemented using the Xilinx Vivado Design Suite® to create distinguishable current distributions on the FPGAs for measurement by the QDM. Clusters of three-inverter ring oscillators are synthesized, placed, and routed to four different predefined clock regions on the FPGA, with clear spatial separation and spanning a majority of the die surface as shown in Fig. 2(c). A cross section of the die is shown in Figs. 2(d) and 2(e). The clusters consist of variable numbers of ring oscillators, allowing for incremental increase or decrease of the current draw at the different locations on the FPGA. The active states of the FPGA are defined by ring oscillator clusters implemented in one of the predefined regions, and the idle state is defined as the FPGA powered on with no implemented ring oscillators. These active and idle states of the FPGA are used to create
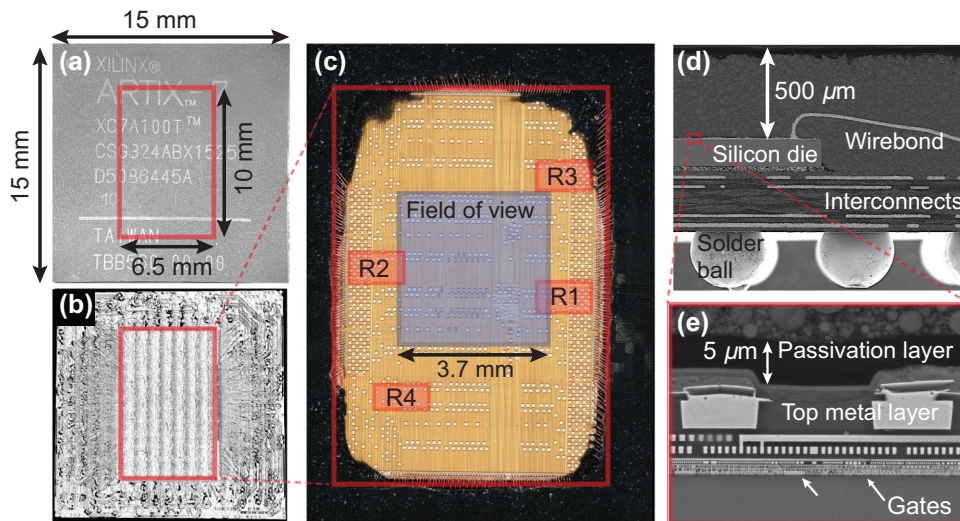

FIG. 2. (a) Intact Xilinx 7-series Artix FPGA with die location and dimensions indicated in red. (b) X-ray image of the FPGA package determining the position and size of die outlined in red. (c) A high-resolution image of the decapsulated FPGA with the fixed diamond measurement field of view indicated with a blue box, and the location of ring oscillator clusters indicated by red boxes labeled R1–R4. (d) Scanning electron microscope (SEM) image of the FPGA cross section showing the 500 μm standoff distance between the chip die and the top layer. (e) Close-up of the SEM focusing on the metal layers of die. The thickness of the passivation layer is 5 μm and sets the minimum standoff distance for the decapsulated measurements.

a lock-in type measurement of the chip activity. The ordering of states during a series of measurements is randomized to reduce susceptibility to systematic noise sources.

C. Experimental protocol and data analysis

CW ODMR measurements are taken with the FPGA in both active and idle states. The duration of each measurement is approximately 5 min per N-V axis for each state (see the Supplemental Material [35]). Such extended measurements are insensitive to transient effects on time scales shorter than the measurement, and sensitive to environmental drifts on the time scale of the measurement. Magnetic field contributions from the ring oscillators are determined by subtracting the measured idle state ODMR frequencies from the measured active state ODMR frequencies, yielding the overall magnetic field due to the ring oscillators alone. For such measurements, the N-V ground-state Hamiltonian is given by

$$H/h \approx \left(D + \frac{\partial D}{\partial T}\Delta T + M_z\right)S_z^2 + \gamma(B_z + \Delta B_z)S_z$$
$$+ \gamma(B_x + \Delta B_x)S_x + \gamma(B_y + \Delta B_y)S_y. \quad (3)$$

Here, terms with Δ originate from the FPGA active states and $\partial D/\partial T \approx -74$ kHz/°C [41]. Following these definitions and treating the off-axis magnetic fields as perturbative, the idle and active state resonant frequencies for the upper (f_+) and lower (f_-) transitions of a single N-V axis (i) are given by [38]

$$f_{\pm,i,\text{idle}} \approx (D + M_z) + \frac{3\gamma^2}{2D}(B_x^2 + B_y^2) \pm \gamma B_z \quad (4)$$

and

$$f_{\pm,i,\text{active}} \approx \left(D + \frac{\partial D}{\partial T}\Delta T + M_z\right)$$
$$+ \frac{3\gamma^2[(B_x + \Delta B_x)^2 + (B_y + \Delta B_y)^2]}{2(D + \frac{\partial D}{\partial T}\Delta T + M_z)}$$
$$\pm \gamma(B_z + \Delta B_z). \quad (5)$$

The desired FPGA state-dependent magnetic field projection on each N-V axis, $\Delta B_{z,i}$, and the change in local temperature, ΔT, are given by

$$\Delta B_{z,i} = \frac{1}{2\gamma}(\Delta f_{+,i} - \Delta f_{-,i}),$$
$$\Delta T = \frac{1}{2\frac{\partial D}{\partial T}}(\Delta f_{+,i} + \Delta f_{-,i}), \quad (6)$$

where $\Delta f_{\pm,i} = f_{\pm,i,\text{active}} - f_{\pm,i,\text{idle}}$. The off-axis magnetic fields of the sample are suppressed by the zero-field splitting; thus, terms dependent on ΔB_x and ΔB_y are sufficiently small to be neglected in Eq. (6) (see the Supplemental Material [35]). Terms dependent on B_x, B_y, B_z,

D, and M_z are canceled by subtracting the idle resonance frequencies from the active state resonance frequencies. Determining the resonance frequencies from all four N-V orientations for vector measurements, labeled $i = 1, 2, 3, 4$ in Fig. 1(d), enables solving for the vector magnetic field in the lab frame:

$$\Delta B_X = \frac{\sqrt{3}}{2\sqrt{2}}(\Delta B_{z,2} + \Delta B_{z,4}), \quad (7a)$$

$$\Delta B_Y = \frac{\sqrt{3}}{2\sqrt{2}}(\Delta B_{z,1} + \Delta B_{z,3}), \quad (7b)$$

$$\Delta B_Z = \frac{\sqrt{3}}{4}[(\Delta B_{z,1} - \Delta B_{z,3}) - (\Delta B_{z,4} - \Delta B_{z,2})]. \quad (7c)$$

Recall that X, Y, and Z are the laboratory frame coordinates; see Fig. 1(b).

The ODMR lineshape for N-V ensembles is well described by a Lorentzian lineshape [38,42]. ODMR spectra for vector measurements of a ^{14}N diamond sample contain 24 resonance features (three hyperfine features times two electronic spin transitions times four N-V axes); see Fig. 1(d). The resonance frequencies of Eq. (6) are extracted from the data by fitting all the Lorentzian parameters for every pixel in the field of view [16]. Furthermore, the contrast and linewidth [43] of the resonances are determined, giving additional state-dependent information (see the Supplemental Material [35]) that can additionally be used for probing high-frequency magnetic fields [44]. GPU-based fitting algorithms [45] speed up this computationally intensive fitting and enable rapid analysis of a large number of measurements.

III. RESULTS

A. Vector magnetic imaging

In Fig. 3(a) we show QDM vector magnetic field images measured on the decapsulated FPGA for clusters of $N = 200$ ring oscillators in two of the predefined regions indicated in the Vivado floor planner, labeled R1 and R2 in Fig. 2(c). The vector magnetic field images are derived from CW ODMR measurements using Eqs. (6) and (7). Observed maximum magnetic fields are on the order of approximately 15 μT with a noise floor of approximately 20 nT (see the Supplemental Material [35]). Spatial variation of the magnetic field is located on the right of the field of view for R1 and on the left for R2. This localization corresponds to the positions of R1 and R2 on the Vivado floor planner, indicating that high current densities for power distribution are concentrated to the region of activity on the die. The vector magnetic field measured in the idle state with zero ring oscillators, shown in the bottom row of Fig. 3(a), reveals the structure of the ball grid array that connects the FPGA to the Digilent board. The state-dependent magnetic fields owing to the ring oscillator

current densities [see Eq. (7)] are thus measured in superposition with the spatially inhomogeneous field resulting from the ball grid array.

The presence of a nonzero B_Y component in R1 and R2, as seen in Fig. 3(a), indicates contributions to the magnetic field from current density sources that run underneath and perpendicular to the visible traces of the top metal layer. These sources are likely a combination of currents in the lower layers of the metal stack and in the interconnects between the wirebonds and ball grid array seen in the SEM image in Fig. 2(d). Discontinuities present in the B_X and B_Z fields indicate a change of the current direction guided by through-silicon vias in the Z direction that connect the different, stacked metal layers. Regions R3 and R4, seen in Fig. 2(c), are both outside the measurement field of view. However, in both cases, state-dependent current is measured in locations corresponding to the direction of current flow in the appropriate location on the die (see the Supplemental Material [35]). This demonstrates the possibility to determine circuit activity outside of the diamond periphery by observing correlated magnetic fields within the nominal field of view.

An optical image of the die through the diamond is used to spatially align the magnetic field measurement with the high-resolution optical images taken of the decapsulated chip. Spatial variation of the B_X and B_Z magnetic field components corresponds well with the physical features of the top metal layer. In Fig. 3(b) we show an enlarged overlay of the B_Z field for 200 ring oscillators in R1 with the optical image of the die, demonstrating feature alignment. Distinct features are visible in the fields that correspond to physical structures, including bends in the wires labeled (i) and (ii) in the figure. Some features in the magnetic field map do not correspond to any visible features on the top metal layer, such as the magnetic trace indicated by (iii) or the discontinuity in field direction indicated by (iv). Visualization of the magnetic field data along a single dimension across the field of view (see the Supplemental Material [35]) further illustrates the detailed spatial features present in the different magnetic field vector images. These fields suggest the presence of additional current routing by vias and other structures below the plane of the top metal layer.

B. Single N-V axis magnetic imaging

Single N-V axis QDM measurements [16] are used to collect a large data set of magnetic field images from ring oscillator clusters for classification. These data are taken by monitoring the outermost ODMR spectral features ($f_{-,1}$
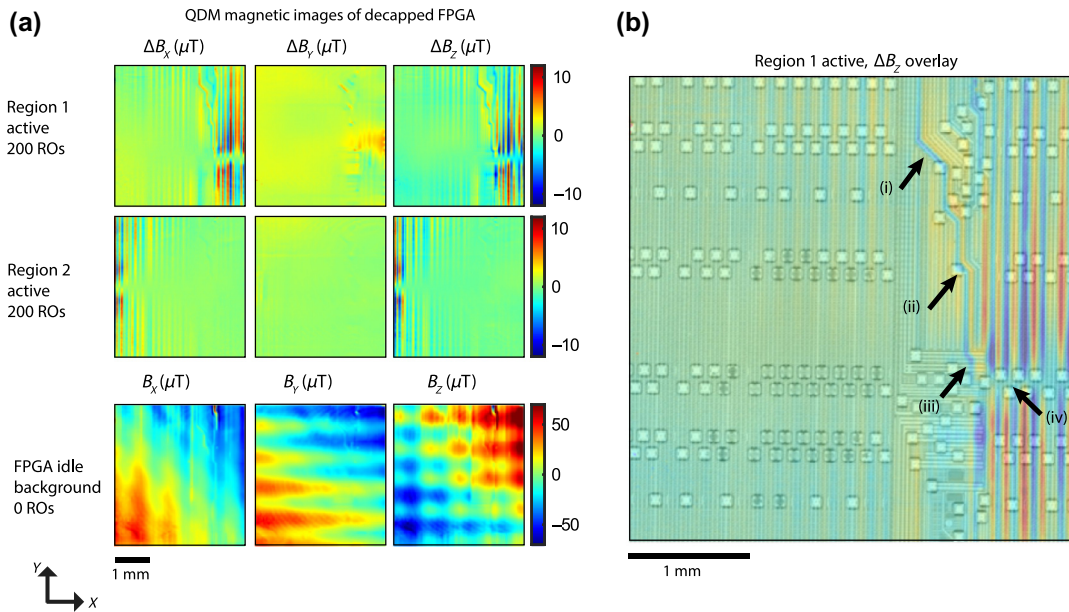

FIG. 3. (a) QDM vector magnetic field maps of the decapped FPGA for different ring oscillator (RO) clusters activated in regions R1 and R2. The location of the 3.7×3.7 mm^2 diamond field of view is fixed on the FPGA for all magnetic field images [see Fig. 2(c)]. State-dependent magnetic field changes (ΔB_X, ΔB_Y, ΔB_Z) are calculated by subtracting background idle magnetic field images from active magnetic field images. Wires on the top metal layer are generally oriented in the Y direction, yielding prominent ΔB_X and ΔB_Z fields. ΔB_Y magnetic field maps show contributions from deeper sources. Background magnetic field maps of the idle FPGA with zero ring oscillators show variations of the field from the mean. Several different background fields are evident: a gradient from the bias magnet, distortion of the bias field from the ball grid array, and background current delivery. (b) The ΔB_Z data for 200 ring oscillators in R1 plotted in transparency over a high-resolution optical image of circuit die. Regions of interest discussed in the text are indicated by (i), (ii), (iii), and (iv).

and $f_{+,1}$) with the same bias field in the lab frame, and the laser polarization and microwaves optimized for the N-V axis being monitored to improve measurement contrast [16]. Projection imaging is useful for large data acquisition due to the speedup in measurement time; however, the vector nature of the field is not captured. The laser polarization and microwaves are optimized for the single N-V axis being monitored. Measuring only a single pair of resonance features results in about a $4\times$ speed up by reducing the number of swept microwave frequencies by a factor of four.

In Fig. 4(a) we show example projection magnetic field images, averaged over ten measurements, for 5, 50, and 200 ring oscillators in regions 1 and 2 for the decapsulated FPGA and the intact FPGA. Magnetic fields are generally reduced with diminishing numbers of ring oscillators, owing to the smaller current densities required for power distribution to smaller clusters. The maximum field amplitude is found not to scale linearly with the number of ring oscillators due to the currents being distributed over a differing number of wires on the top metal layer. The approximately 200 nT magnetic field arising from a single ring oscillator is detectable for the decapsulated chip [Fig. 4(b)] given the experimental noise floor of 20 nT

(see the Supplemental Material [35]). The overlay of the measured magnetic field and the top metal layer illustrates potential location of vias where current is routed to deeper metal layers.

Magnetic fields measured for the intact chip are decreased in magnitude and have lower intrinsic spatial resolution due to the large standoff distance, compared to the decapsulated chip. The suppression of higher spatial frequency signals at large standoff distances allows for more aggressive binning and spatial filtering of the intact data, without sacrificing spatial resolution and field information (see the Supplemental Material [35]). This approach enables a lower noise floor of 2 nT for the intact chip data, which partially overcomes the reduction of field amplitude with distance. For some regions of the field of view, the noise floor is limited by state-independent variation in the magnetic field (see the Supplemental Material [35]) likely due to long-time power instability of the board. In order to enhance sensitivity and push the speed at which measurements can be taken, diamonds with thicker N-V layers can be utilized to increase total fluorescence at the cost of spatial resolution (see the Supplemental Material [35]). Such methodology may be especially beneficial when performing intact measurements, where the
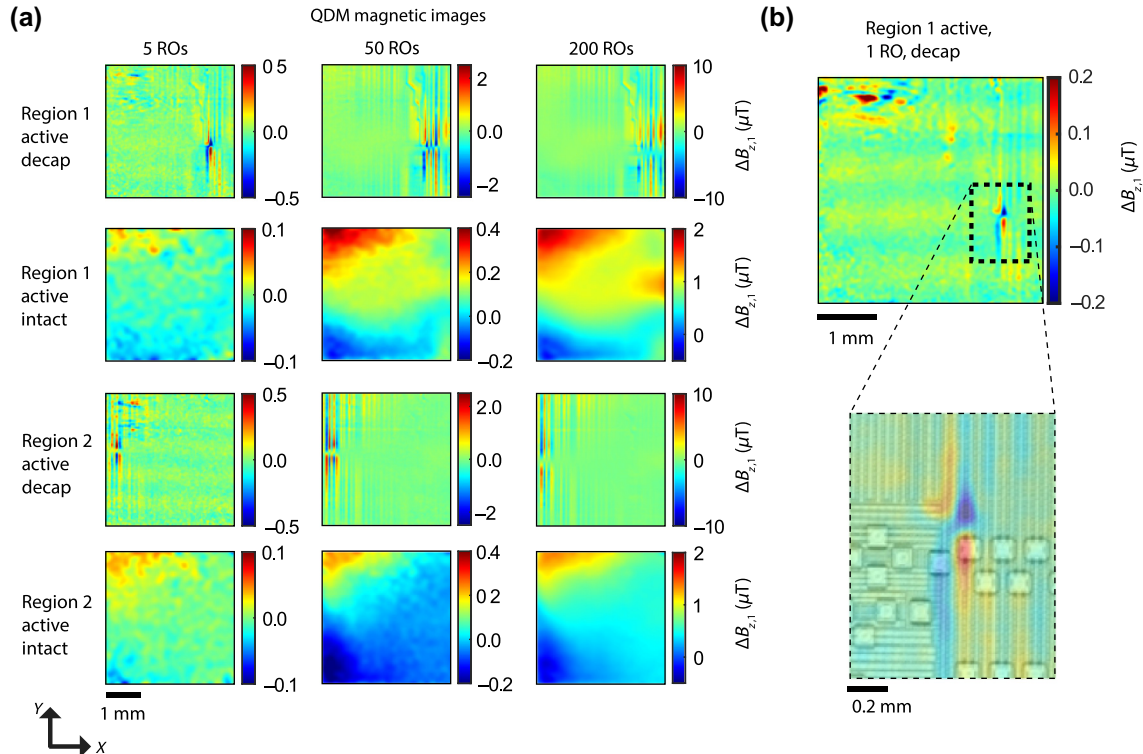

FIG. 4. (a) QDM magnetic images indicate sensitivity to changing the number of ring oscillators in different regions for the decapsulated (decap) and intact chips when performing overlapped measurements. Different scale bars are used for feature clarity. (b) Decapsulated QDM data of $\Delta B_{z,1}$ for a single active ring oscillator in region 1, demonstrating measurement sensitivity to the magnetic field from current supplying a single ring oscillator. Inset: Overlay of the magnified single ring oscillator magnetic field image with a high-resolution optical image of the circuit die. Each image is the average of 10 QDM (nominally identical) measurements.

spatial resolution is already limited by the package standoff distance.

The dependence of current on the ring oscillator cluster size leads to state-dependent temperature changes of the FPGA, which are determined from N-*V* ODMR measurements using Eq. (6). Because of the high thermal conductivity of the diamond chip, there is no spatial structure in the resultant temperature maps. However, from temperature measurements over the entire field of view, we are able to determine a scaling of approximately $0.0075\,^{\circ}$C per active ring oscillator (see the Supplemental Material [35]), with a temperature increase of approximately $1.5\,^{\circ}$C for the 200 ring oscillator state.

C. Magnetic field source interpretation

The QDM magnetic field images shown in Figs. 3 and 4 result from current density sources located at various depths in the decapped and intact FPGAs. Current is distributed in the interconnect layers of the silicon die and the package substrate. Each layer acts as a quasi two-dimensional current source contributing to the overall magnetic field detected by the N-*V*s. The standoff distance between the N-*V* sensing plane and the current sources determines which metal layer dominates the field measurement. Generally, small wire features close to the sensing plane will dominate for small standoff distances and large wire features far from the sensing plane will dominate for large standoff distances.

For example, the 21 μm wide wires of the top metal layer contribute to the measured ΔB_X and ΔB_Z fields in the QDM images of the decapped FPGA, as seen by the spatial features of the fields in Fig. 3. Topside decapsulation removes the 500 μm of epoxy packaging above the die shown in the SEM in Fig. 2(e). This results in a 5–10 μm standoff distance between the top metal layer and the N-*V* sensing plane that is sufficiently small to resolve the spatial variation of fields resulting from currents in the top metal layer. Fields from smaller wires in the metal stacks below the top metal layer are too distant to contribute significantly to the measured field.

The measured magnetic field distributions for both the decapsulated and intact chips include contributions from large current sources far from the N-*V* sensing plane. These sources consist primarily of the metal layers of the 400 μm thick package substrate. The 300 μm silicon die separates the N-*V* layer from the top of the package substrate for the decapsulated chip. An additional separation of approximately 500 μm due to the epoxy gives a total standoff distance of about 800 μm for the intact chip. These large current sources result in the broad features of the measured ΔB_Y data for the decapsulated chip in Fig. 3(a), and of the measured $\Delta B_{z,1}$ for the intact chip in Fig. 4(a). The dominant contribution of the substrate layers explains

differences in the measured fields of the intact chip compared to those of the decapsulated chip, even when the latter are low-pass filtered to account for the difference in measurement standoff.

Comparison of the measured data with finite element analysis simulations support the interpretation of the data as resulting from contributions of current sources in different layers at different depths from the N-*V* plane. The finite element analysis model, constructed in COMSOL Multiphysics®, consists of 21.6 μm wires in the top metal layer with inter-wire spacing of 12.7 μm, and 100 μm thick metal wires in the package substrate layer with interwire spacing of 100 μm. An interlayer separation of 300 μm represents the thickness of the silicon die. A current of approximately 10 mA is applied to the wires in each layer with alternating bias to approximate the current of 200 active ring oscillators. Plots of B_Z for planes at 25 μm and 500 μm above the top metal layer are given (see the Supplemental Material [35]) for comparison with the N-*V* measurements at the nominal standoff distances for decapsulated and intact chips, respectively. The spatial features of the small wires are only evident in the B_Z field of the plane with small standoff, whereas the contribution of the large wires dominates at large standoff distances.

The measurements presented in Figs. 3 and 4 are the net static magnetic fields resulting from steady-state ring oscillator operation in the FPGA. The static fields are interpreted to result from a time-averaged superposition of dynamic current draws from the top metal layer to the transistor level. The ring oscillators used for this experiment each consist of three CMOS inverters that sequentially switch state during ring oscillator operation. A small, short-circuit current spike occurs in every inverter that switches state (due to simultaneous conduction through the two transistors of the inverter inducing a transient current path from the supply voltage to the ground). However, the individual switching of the inverters in the ring oscillators is not temporally synchronized, resulting in a time-averaged, steady-state current draw from the top metal layer, and a consequently measurable static magnetic field (see the Supplemental Material [35]).

IV. ANALYSIS

Forward modeling of the current distributions and resulting magnetic fields for the different ring oscillator states programmed on the FPGA is an intractable problem without complete knowledge of the wire layout and current paths. Interpretation of the QDM measurements by comparison with forward-model simulations is therefore limited to the arguments, such as those presented in the previous section. However, automated machine learning algorithms can be applied to the QDM data to discriminate between and ultimately classify the different operating states. Ideally, a magnetic field image is used as input to

a machine learning algorithm, and the functional state, defined as the number of active ring oscillators in this initial demonstration, is determined as the output. In practice, this problem is approached with a limited data set of magnetic field images for each FPGA state, and a dimensionality reduction algorithm is employed before applying a classification technique using the PYTHON [46] package `scikit-learn` [47].

A. Data preprocessing

QDM data undergoes a series of preprocessing steps in preparation for dimensionality reduction and classification. Only images with region 1 active are used so that the number of ring oscillators is predicted by the classification scheme. The number of ring oscillators activated for any given image is one of 0, 1, 5, 10, 50, 100, or 200. The data set consists of 40 QDM images per ring oscillator state for the decapsulated chip and 32 images per ring oscillator state for the intact chip. These $M \times N$ images are subsequently binned such that the decapsulated images contain 600×606 pixels and the intact images contain 300×303 pixels, while covering the same field of view. Measurements of the idle state (zero ring oscillators) are randomly taken during data collection to account for long-term drifts. These idle state measurements are subtracted from active state images nearest in time. The intact and decapsulated data sets are split into training and test sets so that the prediction accuracy of the trained model can be estimated on data that the training procedure has not encountered. The splits are 75%/25% for the decapsulated images and 64%/36% for the intact images.

B. QDM image dimensionality reduction

Each magnetic field image is composed of approximately 10^5 pixels and thus occupy a high-dimensional space for classification. Principal component analysis [48, 49] (PCA) is therefore used to reduce the dimensionality of the classification problem. PCA is a well-established technique that determines the highest variability axes of a high-dimensional data set. PCA amounts to an eigenanalysis where the eigenvectors, called principal components, correspond to the axes of interest, and the eigenvalues relate to the amount of data variance along the respective principal components.

PCA is applied separately to the data sets of the decapsulated chip and the intact chip with the `scikit-learn` class `decomposition.PCA()` and yields principal components such as those plotted in Fig. 5(a). Spatial patterns evident in the principal components are also present in the magnetic field images of Fig. 4(a), confirming that these features are physically significant and important for distinguishing between different samples. There exist as many principal components as dimensions in the data set;

however, only the first several principal components capture non-noise-based information (see the Supplemental Material [35]). We determine that greater than 99% of the variance in the intact and decapsulated data sets is captured by the first nine principal components, which are therefore the only principal components used in this analysis.

The scores of these first nine principal components are used to effectively reduce the dimensionality of the magnetic field images from approximately 10^5 pixels to nine scores. The principal component scores, $S^{i,j}$, are determined by taking the dot product of the ith principal component, defined as $\mathbf{W}^i$, with the jth image, $\mathbf{B}^j$, and normalized by the total number of pixels. This gives

$$S^{i,j} = \frac{1}{MN} \sum_{m=1}^{M} \sum_{n=1}^{N} W_{m,n}^i B_{m,n}^j \tag{8}$$

for the first nine principal components. In Fig. 5(b) we show examples of the PCA scores: the score for PC1 is plotted against the score for PC2 for each magnetic field image of both the decapsulated and intact data (additional principal components and score plots are given in the Supplemental Material [35]). The plot is color coded by the number of active ring oscillators, showing that these two scores are useful in distinguishing the number of active ring oscillators on the FPGA for both decapsulated and intact measurements. Classification of the active number of ring oscillators is accomplished by using the first nine PCA scores as input to a support vector machine (SVM) classifier algorithm. The spread of data points along a fixed slope for each state in Fig. 5(b) is consistent with small offsets between different image acquisitions (see the Supplemental Material [35]).

C. Integrated-circuit activity state classification

A support vector machine [50] (SVM) is the supervised classification technique used to classify the magnetic field images, leveraging their key features characterized by the PCA scores. SVMs are a set of algorithms that seek to classify samples by creating a boundary between categories of a training data set that maximizes the gap separating those categories. Samples from a test set are then classified in relation to this boundary.

The `scikit-learn` class `svm.SVC()` is used as a multidimension, multicategory classifier. The categories for classification are the chip states given by the number of ring oscillators. The dimensionality is given by the nine PCA scores recorded for each image. PCA scores are fit to the known FPGA states with a linear SVM model and a regularization parameter of $C = 6$ (see the Supplemental material [35]).
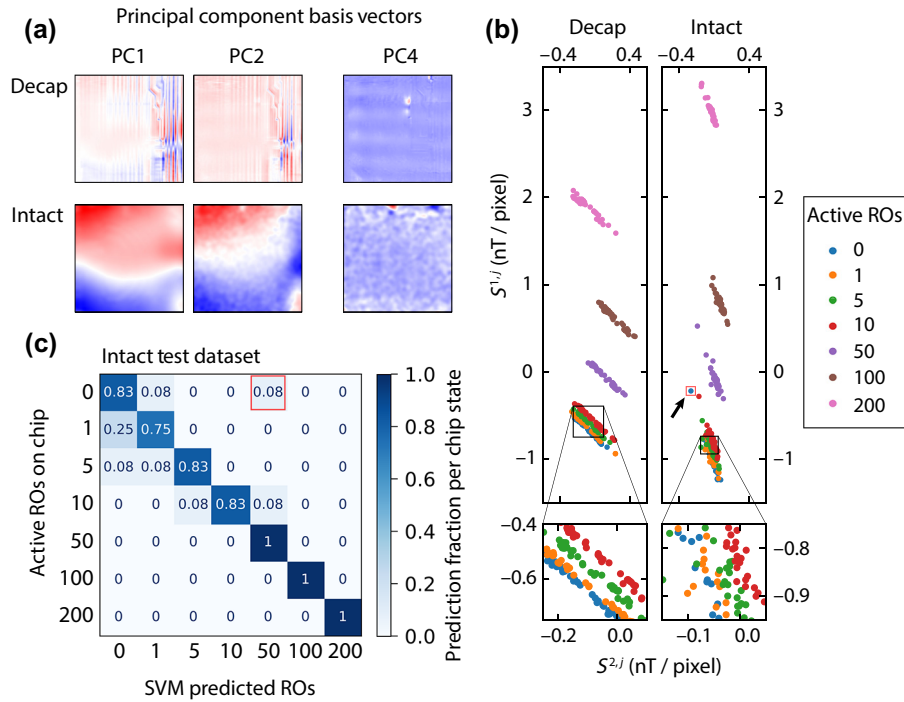
FIG. 5. Principal component analysis and support vector machine classification of QDM images. Region 1 is active with 0, 1, 5, 10, 50, 100, or 200 ring oscillators. (a) Example principal component basis vectors plotted as images for both decapsulated (labeled "decap" in the figure) and intact data sets. PC1 and PC2 are shown to exemplify principal components that resemble magnetic field images and thus will be useful in chip state classification. PC4 is shown as an example principal component that captures activity state-independent variations and thus will not be useful in chip state classification. (b) The PCA score for PC1, $S^{1,j}$, is plotted against the score for PC2, $S^{2,j}$, for each magnetic field image, $\mathbf{B}^j$, as a demonstration of state distinguishability . This distinguishability is evidenced by the separation of colors representing differing numbers of active ring oscillators. Insets magnify the scores for small numbers of ring oscillators, and show greater fidelity of state separation in the decapsulated data set compared to the intact data set. (c) Table of SVM predictions on the test set for the intact images. For each unique value of active ring oscillators, there are 12 images in the test set. Rows indicate the fraction of images predicted for each of the possible chip states. All but one prediction [indicated by the red boxes in (b) and (c)] lie on or near the main diagonal, demonstrating the high predictive power of the SVM classifier. The corresponding table for the decapsulated data set is not shown, as the main diagonal would contain 1's and the off diagonals would contain 0's owing to the perfect separability of each state (see Table I).

D. Classification results

The full machine learning model, including preprocessing, PCA, and SVM, is fit using the training set and subsequently evaluated on the test set for both decapped and intact FPGA data. A prior step of cross validating the model hyperparameters is taken for the intact FPGA data set (see the Supplemental Material [35]). The machine learning model efficacy, summarized in Table I, is determined by the accuracy of the test set evaluations. FPGA activity states are well separated in PCA space for the decapsulated data set. Predictions on the test set consequently yield perfect accuracy, even for small numbers of ring oscillators, consistent with expectations (see the Supplemental Material [35]).

Results for an intact data set are similarly well separated for large numbers of ring oscillators, resulting in perfect prediction accuracy for greater than or equal to 50 ring oscillators. However, FPGA activity states are not fully separated for less than 50 ring oscillators, resulting in imperfect predictions. Nonetheless, the trained machine learning model achieves approximately 80% accuracy for each of 0, 1, 5, and 10 ring oscillator active states. In Fig. 5(c) we additionally show that incorrect predictions are nearly always close to the correct state. For example, the model predicts five ring oscillators correctly in 83% of test cases, with misclassifications of zero or a single ring oscillator otherwise. The red box in Fig. 5(c) indicates a single case for which the classifier incorrectly predicts 50 ring oscillators for a zero ring oscillator state. An arrow and analogous red box in Fig. 5(b) shows that the PCA score for this state is an outlier in the data.

The positive classification results presented in Fig. 5 give an initial demonstration of the capability of combined QDM and machine learning techniques to identify integrated-circuit activity via noninvasive magnetic field imaging. The present results using ring oscillators are

TABLE I.   Chip state prediction accuracy on the test dataset.

	Number of ROs (region 1)							Total
	0	1	5	10	50	100	200	
Decapsulated	1.00	1.00	1.00	1.00	1.00	1.00	1.00	1.00
Intact	0.83	0.75	0.83	0.83	1.00	1.00	1.00	0.89

also potentially translatable to approaches that use the power side channel for chip activity analysis [51–53]. An extended dataset (see the Appendix) is taken to further elucidate the benefit of a large number of measurements per state on the prediction accuracy. Furthermore, in the extended dataset, the definition of state for the purpose of classification is expanded to include both the number of ring oscillators and region activated (see the Appendix). This dataset is also used to determine the impact of measurement standoff distance on the ability to discriminate between spatially separated activity on the integrated circuit. The extended dataset is analyzed with the state classification criteria defined to include the spatial location of the active region in addition to the number of ring oscillators per region. For a simulated measurement standoff distance of $\Delta z = 500$ μm, similar to that between the N-V layer and FPGA current sources in the intact chip, a classification accuracy of greater than 98% is achieved on the extended dataset using 100 samples per state (see the Appendix). This result indicates that a high degree of spatial state classification is possible in addition to local power classification using a large number of samples per state. Large data sets, such as the one presented in the Appendix, combined with more powerful machine learning methods have promise to enable classification of a wide array of chip activity in the context of hardware security and fault detection.

V. OUTLOOK

We present a demonstration of N-V diamond imaging of the static magnetic field emanations from a FPGA. The ensemble N-V measurement technique of the QDM yields simultaneous wide field of view (few millimeters) with high resolution (approximately 10 μm) vector magnetic field images, which is not achievable using other techniques. We further demonstrate that these images can be used with machine learning techniques to quantifiably determine the active state of the FPGA integrated circuit, for both decapsulated and intact chips. The fidelity of classification is dependent on the activity level and the standoff distance between the circuit currents and the measurement plane. Our results show conclusively that it is possible to use static magnetic field measurements to identify targeted, active states on a FPGA without requiring time domain data.

The long-term goal of the combined QDM imaging and machine learning technique is to augment state-of-the-art diagnostic techniques in areas such as fault detection, Trojan detection, counterfeit detection, watermarking, and electromagnetic side channel characterization. In the present work, we show that patterns of magnetic fields from the power distribution network of an integrated circuit are a significant indicator of steady-state chip activity. In future work, the simultaneous widefield and high-resolution magnetic imaging provided by the QDM may enable detection of correlated spatial and temporal (e.g., transient) events over sequential measurements, which is not possible with scanning magnetometry techniques.

Technical improvements enabling faster QDM measurements [15,36,54–56] will also be implemented in future work for extended data collection and further analysis techniques. Examples of such improvements include development and utilization of higher quality diamond material [57] with thinner layers of N-Vs to enable better spatial resolution, faster measurements through utilization of fewer microwave frequencies in CW ODMR lock-in measurements [23], pulsed dc magnetometry protocols such as Ramsey magnetometry [38], and utilization of cameras with deeper wells and faster data transfer times. Larger data sets will allow for leveraging the full power of convolutional neural networks for advanced state classification. Time-resolved measurements will also permit discrimination of magnetic fields by temporal or frequency profiles. It is possible such measurements could be used to resolve the magnetic fields specific to adjacent circuitry, for example, from clock and power distribution networks as well as gate level activity, providing further indication of chip activity. The unique capabilities of N-V diamond magnetic field imaging thus have great promise for integrated-circuit applications.

APPENDIX: EXTENDED DATASET

An extended dataset of magnetic field images is additionally collected. This extended dataset further elucidates the impact of the number of measurements per state on the prediction accuracy, as well as the impact of measurement standoff distance on the ability to discriminate between spatially separated activity on the integrated circuit. Two proximal regions, defined as region 5 (R5) and region 6 (R6) are used to further test spatial discrimination capabilities of PCA and SVM. The data consist of 100 measurements taken per state on the decapsulated chip for 12 different states. The states are composed of clusters of 0, 2, 4, or 6 ring oscillators that are activated in R5, or R6, or simultaneously in both R5 and R6.

The effect of measuring at different standoff distances is simulated using upward continuation [14] to calculate the expected magnetic field at a large standoff distance, Δz. In Fig. 6 we show the average of the 100 measurements for 3 of the 12 different states and projections at $\Delta z = 0$ μm (decapsulated dataset), 50 μm, 250 μm, 500 μm (analog to an intact chip), and 1000 μm.

Distinct spatial patterns are evident for the activation of two ring oscillators in R5 and R6. Specifically, a greater number of oscillations in the magnetic field polarity are present in R6 compared to R5. This difference is the result of different routing of power distribution in the top metal layer. Upward continuation of the data results in a decrease in the magnetic field amplitude that occurs more rapidly in R6 as a function of the standoff distance than in R5. This difference is expected due to the cancelation of the large number of oscillating fields from neighboring wires in R6. Even at $\Delta z = 1000$ μm, there is clear spatial distinguishability between all of the states, which is further quantified with PCA and SVM analysis.
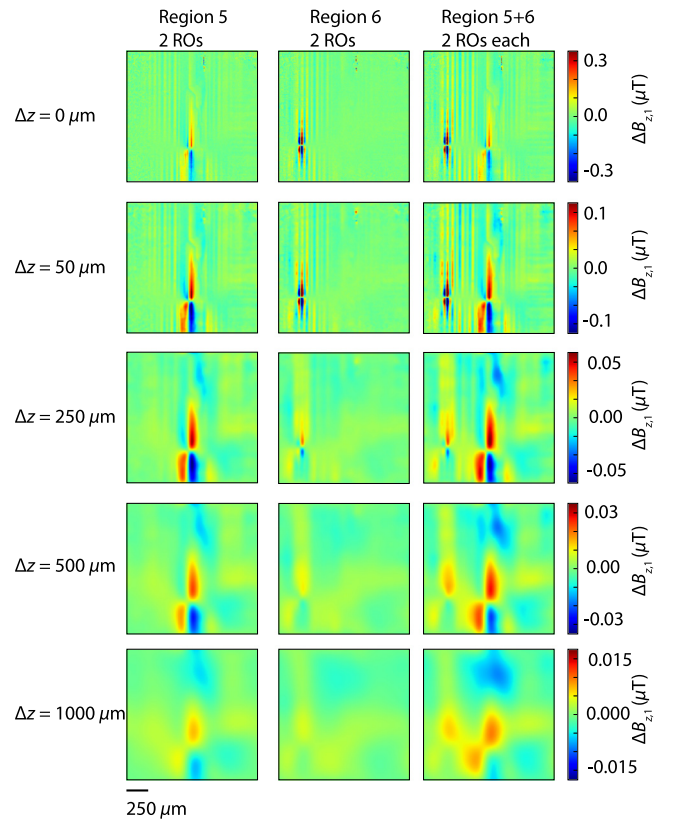

FIG. 6. Subset of the extended QDM magnetic field dataset with two ring oscillators active in region 5, region 6, or region 5 and region 6 simultaneously. The top row is high SNR data of 100 measurements taken from the decapsulated chip. Subsequent rows show the calculated magnetic image at different standoff distances of $\Delta z = 50$ μm, 250 μm, 500 μm, and 1000 μm. The $\Delta z = 500$ μm row is the closest approximation of measurements taken of an intact chip.

The PCA + SVM analysis presented in the main text is performed on the extended dataset. However, in the case of the extended dataset, state classification is determined by the spatial location of the active region in addition to the number of ROs per region. Thus, a correct classification for the purposes of model accuracy consists of correctly identifying both the active region(s) as well as the number of active ring oscillators per active state, i.e., a state is defined as (active region, number of active ROs). Accuracy is defined as the fraction of states correctly classified. The robustness of the dataset is tested by estimating the model accuracy as a function of the dataset size, shown in Fig. 7(a). The upward continued dataset with $\Delta z = 500$ μm is used and the size of the dataset is varied from 10 samples per state to 100 samples per state. A train-test split of 64%/36% is used to mimic the analysis of the intact dataset in the main text. The training set has 100% accuracy when the number of samples per state is less than 60, but dips slightly below 100% for larger datasets. This is expected since the algorithm complexity is fixed but

(a) $\Delta z = 500\ \mu m$

(b) 100 samples per state

(c)

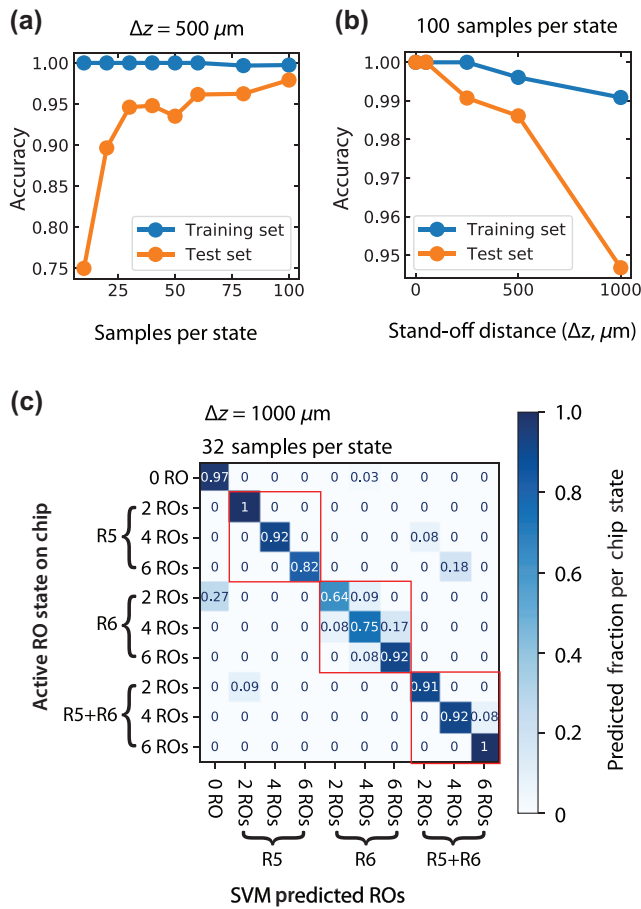$\Delta z = 1000\ \mu m$

32 samples per state

FIG. 7. PCA + SVM model performance metrics of the extended dataset. (a) Model accuracy is plotted as a function of the size of the dataset for both the training and test sets. A stand-off distance of 500 μm is chosen to most closely replicate the intact dataset in the main text. (b) Model accuracy is plotted as a function of the standoff distance. The full dataset is used (100 samples per state). (c) Matrix of state predictions versus active state on chip at a standoff distance of 1000 μm. The matrix is row normalized to 1 so that each element represents the fraction of measurements of a given state that are predicted to be any state. The red boxes enclose predictions for which the predicted region and active region are the same.

chip and the decapsulated chip is about 500 μm of package material and thus $\Delta z = 500\ \mu$m is the best estimate for an analogous dataset taken from an intact chip. In Fig. 7(b) we show the model accuracy as a function of the standoff distance when the entire dataset is used (100 samples per state). As expected, perfect classification is achieved for small standoff distances and monotonically decreases in accuracy with increasing standoff distance. Importantly, for $\Delta z = 500\ \mu$m, greater than 98% accuracy is achieved on the test set, implying that an analogous intact dataset would have a high degree of spatial state classification in addition to local power classification.

Finally, to further elucidate the ability to perform spatial classification, the state-by-state predication rates are shown in Fig. 7(c). Results with 32 samples per state are shown to mimic the dataset analyzed in the main text. A standoff distance of $\Delta z = 1000\ \mu$m is chosen to show that prediction errors occur in accordance with expectations. In Fig. 7(c) we present the fraction of images with a given state that are predicted to be each possible state. Most predictions lie on the main diagonal as the overall accuracy is about 89%. The red boxes show states from one region that are predicted to be in the same region. The majority of misclassifications are expected to lie in these red boxes. This is clearly the case, especially for region 6. In this region, two ring oscillators are misclassified as either zero ring oscillators or four ring oscillators from the same region. Four ring oscillators are misclassified as either two or six ring oscillators, and six ring oscillators are misclassified as four ring oscillators. The fact that this region has the highest error rate is consistent with expectation because the features in this region become less distinguishable as the standoff distance increases. Most of the remaining misclassifications are between R5 and regions R5 + R6, which is expected since these regions look visually similar, as seen in Fig. 6.

the absolute deviations in the data increase with sample size. Despite the increased error rate in the training set for larger samples per state, the larger datasets allow the model to learn the underlying structures of the dataset and consequently generalize better to unseen data. Thus, the accuracy increases from 75% at 10 samples per state to 97% with 100 samples per state. Beyond 30 to 40 samples per state, the accuracy begins to level off, suggesting that 100 samples per state is enough data to get the maximum benefit from the PCA + SVM model.

The analysis is performed at various standoff distances to test the predictive power of the model at varying levels of signal degradation. The difference between the intact

[1] M. Rostami, F. Koushanfar, and R. Karri, A primer on hardware security: Models, methods, and metrics, Proc. IEEE **102**, 1283 (2014).

[2] M. Tehranipoor, H. Salmani, X. Zhang, M. Wang, R. Karri, J. Rajendran, and K. Rosenfeld, Trustworthy hardware: Trojan detection and design-for-trust challenges, Computer **44**, 66 (2010).

[3] Semiconductor Industry Association, Winning the battle against counterfeit semiconductor products, SIA Whitepaper, Washington DC (2013).

[4] P. Hoeper and J. Manferdelli, DSB task force on cyber supply chain, Defense Science Board Washington DC USA (2017).

[5] U. Guin, K. Huang, D. DiMase, J. M. Carulli, M. Tehranipoor, and Y. Makris, Counterfeit integrated circuits: A rising threat in the global semiconductor supply chain, Proc. IEEE **102**, 1207 (2014).

[6] J. Balasch, B. Gierlichs, and I. Verbauwhede, in *2015 IEEE International Symposium on Electromagnetic Compatibility (EMC)* (IEEE, 2015), Vol. 246.

[7] J. Gaudestad and A. Orozco, Magnetic field imaging for non destructive 3d IC testing, Microelectron. Reliab. **54,** 2093 (2014).

[8] Y. Tagro, J. J. Yan, D. F. Kimball, H. Ghajari, and D. F. Sievenpiper, in *GOMACTech* (MaXentric Technologies LLC, San Diego, United States, 2017).

[9] A. Orozco, J. Gaudestad, N. Gagliolo, C. Rowlett, E. Wong, A. Jeffers, B. Cheng, F. C. Wellstood, A. B. Cawthorne, and F. Infante, 3d Magnetic Field Imaging for Non-Destructive Fault Isolation (2013).

[10] A. Orozco, Magnetic Field Imaging for Electrical Fault Isolation (2019).

[11] A. N. Campbell, E. Cole, B. A. Dodd, and R. E. Anderson, in *31st Annual Proceedings Reliability Physics 1993* (IEEE, 1993), Vol. 168.

[12] H. H. Huston and C. P. Clarke, in *Annual Proceedings Reliability Physics 1992* (IEEE, 1992), Vol. 268.

[13] Semiconductor Industry Association, Semiconductor research opportunities, (2017).

[14] B. J. Roth, N. G. Sepulveda, and J. P. Wikswo, Using a magnetometer to image a two-dimensional current distribution, J. Appl. Phys. **65,** 361 (1989).

[15] E. V. Levine, M. J. Turner, P. Kehayias, C. A. Hart, N. Langellier, R. Trubko, D. R. Glenn, R. R. Fu, and R. L. Walsworth, Principles and techniques of the quantum diamond microscope, Nanophotonics **8,** 1945 (2019).

[16] D. R. Glenn, R. R. Fu, P. Kehayias, D. Le Sage, E. A. Lima, B. P. Weiss, and R. L. Walsworth, Micrometer-scale magnetic imaging of geological samples using a quantum diamond microscope, Geochem. Geophys. Geosyst. **18,** 3254 (2017).

[17] J. Taylor, P. Cappellaro, L. Childress, L. Jiang, D. Budker, P. Hemmer, A. Yacoby, R. Walsworth, and M. Lukin, High-sensitivity diamond magnetometer with nanoscale resolution, Nat. Phys. **4,** 810 (2008).

[18] A. Gruber, A. Dräbenstedt, C. Tietz, L. Fleury, J. Wrachtrup, and C. V. Borczyskowski, Scanning confocal optical microscopy and magnetic resonance on single defect centers, Science **276,** 2012 (1997).

[19] J. R. Maze, P. L. Stanwix, J. S. Hodges, S. Hong, J. M. Taylor, P. Cappellaro, L. Jiang, M. V. G. Dutt, E. Togan, A. S. Zibrov, A. Yacoby, R. L. Walsworth, and M. D. Lukin, Nanoscale magnetic sensing with an individual electronic spin in diamond, Nature **455,** 644 (2008).

[20] G. Balasubramanian, I. Y. Chan, R. Kolesov, M. Al-Hmoud, J. Tisler, C. Shin, C. Kim, A. Wojcik, P. R. Hemmer, A. Krueger, T. Hanke, A. Leitenstorfer, R. Bratschitsch, F. Jelezko, and J. Wrachtrup, Nanoscale imaging magnetometry with diamond spins under ambient conditions, Nature **455,** 648 (2008).

[21] L. M. Pham, D. Le Sage, P. L. Stanwix, T. K. Yeung, D. Glenn, A. Trifonov, P. Cappellaro, P. R. Hemmer, M. D. Lukin, H. Park, A. Yacoby, and R. L. Walsworth, Magnetic field imaging with nitrogen-vacancy ensembles, New J. Phys. **13,** 045021 (2011).

[22] M. J. H. Ku, T. X. Zhou, Q. Li, Y. J. Shin, J. K. Shi, C. Burch, H. Zhang, F. Casola, T. Taniguchi, K. Watanabe, P. Kim, A. Yacoby, and R. L. Walsworth, Imaging viscous

flow of the Dirac fluid in graphene using a quantum spin magnetometer, arXiv:1905.10791 (2019).

[23] J. F. Barry, M. J. Turner, J. M. Schloss, D. R. Glenn, Y. Song, M. D. Lukin, H. Park, and R. L. Walsworth, Optical magnetic detection of single-neuron action potentials using quantum defects in diamond, Proc. Natl. Acad. Sci. **113,** 14133 (2016).

[24] A. Nowodzinski, M. Chipaux, L. Toraille, V. Jacques, J.-F. Roch, and T. Debuisschert, Nitrogen-vacancy centers in diamond for current imaging at the redistributive layer level of integrated circuits, Microelectron. Reliab. **55,** 1549 (2015).

[25] D. A. Simpson, J.-P. Tetienne, J. McCoey, K. Ganesan, L. T. Hall, S. Petrou, R. E. Scholten, and L. C. L. Hollenberg, Magneto-optical imaging of thin magnetic films using spins in diamond, Sci. Rep. **6,** 22797 (2016).

[26] D. Le Sage, K. Arai, D. R. Glenn, S. J. DeVience, L. M. Pham, L. Rahn-Lee, M. D. Lukin, A. Yacoby, A. Komeili, and R. L. Walsworth, Optical magnetic imaging of living cells, Nature **496,** 486 (2013).

[27] R. R. Fu, B. P. Weiss, E. A. Lima, R. J. Harrison, X.-N. Bai, S. J. Desch, D. S. Ebel, C. Suavet, H. Wang, D. Glenn, D. Le Sage, T. Kasama, R. L. Walsworth, and A. T. Kuan, Solar nebula magnetic fields recorded in the semarkona meteorite, Science **346,** 1089 (2014).

[28] I. Fescenko, A. Laraoui, J. Smits, N. Mosavian, P. Kehayias, J. Seto, L. Bougas, A. Jarmola, and V. M. Acosta, Diamond Magnetic Microscopy of Malarial Hemozoin Nanocrystals, Phys. Rev. Appl. **11,** 034029 (2019).

[29] E. De Mulder, Ph.D. thesis, Katholieke Universiteit Leuven, 2010.

[30] L. Sauvage, S. Guilley, and Y. Mathieu, Electromagnetic radiations of FPGAs: High spatial resolution cartography and attack on a cryptographic module, ACM Trans. Reconfigurable Technol. Syst. (TRETS) **2,** 4 (2009).

[31] A. Horsley, G.-X. Du, and P. Treutlein, Widefield microwave imaging in alkali vapor cells with sub-100 μm resolution, New J. Phys. **17,** 112002 (2015).

[32] J. M. Schloss, J. F. Barry, M. J. Turner, and R. L. Walsworth, Simultaneous Broadband Vector Magnetometry Using Solid-State Spins, Phys. Rev. Appl. **10,** 034044 (2018).

[33] M. W. Doherty, N. B. Manson, P. Delaney, F. Jelezko, J. Wrachtrup, and L. C. L. Hollenberg, The nitrogen-vacancy colour centre in diamond, Phys. Rep. **528,** 1 (2013).

[34] P. Kehayias, M. J. Turner, R. Trubko, J. M. Schloss, C. A. Hart, M. Wesson, D. R. Glenn, and R. L. Walsworth, Imaging crystal stress in diamond using ensembles of nitrogen-vacancy centers, Phys. Rev. B **100,** 174103 (2019).

[35] See Supplemental Material at http://link.aps.org/supplemental/10.1103/PhysRevApplied.14.014097 for additional information on further measurements, integrated circuit information, magnetometer performance, and machine learning details.

[36] J. F. Barry, J. M. Schloss, E. Bauch, M. J. Turner, C. A. Hart, L. M. Pham, and R. L. Walsworth, Sensitivity optimization for NV-diamond magnetometry, Rev. Mod. Phys. **92,** 015004 (2020).

[37] F. Dolde, H. Fedder, M. W. Doherty, T. Nöbauer, F. Rempp, G. Balasubramanian, T. Wolf, F. Reinhard, L. C. L. Hollenberg, F. Jelezko, and J. Wrachtrup, Electric-field

sensing using single diamond spins, Nat. Phys. **7**, 459 (2011).

[38] E. Bauch, C. A. Hart, J. M. Schloss, M. J. Turner, J. F. Barry, P. Kehayias, S. Singh, and R. L. Walsworth, Ultra-long Dephasing Times in Solid-State Spin Ensembles via Quantum Control, Phys. Rev. X **8**, 031025 (2018).

[39] X. Zhang and M. Tehranipoor, in: *2011 Design, Automation & Test in Europe* (IEEE, 2011), Vol. 1.

[40] M. Mandal and B. C. Sarkar, Ring oscillators: Characteristics and applications, Ind. J. Pure Appl. Phys. **48**, 136 (2010).

[41] V. M. Acosta, E. Bauch, M. P. Ledbetter, A. Waxman, L.-S. Bouchard, and D. Budker, Temperature Dependence of the Nitrogen-Vacancy Magnetic Resonance in Diamond, Phys. Rev. Lett. **104**, 070801 (2010).

[42] V. V. Dobrovitski, A. E. Feiguin, D. D. Awschalom, and R. Hanson, Decoherence dynamics of a single spin versus spin ensemble, Phys. Rev. B **77**, 245212 (2008).

[43] A. Dréau, M. Lesik, L. Rondin, P. Spinicelli, O. Arcizet, J.-F. Roch, and V. Jacques, Avoiding power broadening in optically detected magnetic resonance of single NV defects for enhanced dc magnetic field sensitivity, Phys. Rev. B **84**, 195204 (2011).

[44] L. Shao, R. Liu, M. Zhang, A. V. Shneidman, X. Audier, M. Markham, H. Dhillon, D. J. Twitchen, Y.-F. Xiao, and M. Lončar, Wide-field optical microscopy of microwave fields using nitrogen-vacancy centers in diamonds, Adv. Opt. Mater. **4**, 1075 (2016).

[45] A. Przybylski, B. Thiel, J. Keller-Findeisen, B. Stock, and M. Bates, Gpufit: An open-source toolkit for GPU-accelerated curve fitting, Sci. Rep. **7**, 15722 (2017).

[46] G. van Rossum, *Python tutorial*, Tech. Rep. CS-R9526 (Centrum voor Wiskunde en Informatica (CWI), Amsterdam, 1995).

[47] F. Pedregosa, G. Varoquaux, A. Gramfort, V. Michel, B. Thirion, O. Grisel, M. Blondel, P. Prettenhofer, R. Weiss, V. Dubourg, J. Vanderplas, A. Passos, D. Cournapeau,

M. Brucher, M. Perrot, and E. Duchesnay, Scikit-learn: Machine learning in Python, J. Mach. Learn. Res. **12**, 2825 (2011).

[48] F. R. S. Karl Pearson, On lines and planes of closest fit to systems of points in space, London Edinburgh Dublin Philos. Mag. J. Sci. **2**, 559 (1901).

[49] H. Hotelling, Relations between two sets of variates, Biometrika **28**, 321 (1936).

[50] C. Cortes and V. Vapnik, Support-vector networks, Mach. Learn. **20**, 273 (1995).

[51] P. Kocher, J. Jaffe, and B. Jun, in *Advances in Cryptology — CRYPTO' 99*, edited by M. Wiener (Springer, Berlin, Heidelberg, 1999), p. 388.

[52] S. B. Örs, E. Oswald, and B. Preneel, in *Cryptographic Hardware and Embedded Systems*, edited by C. D. Walter, Ç. K. Koç, and C. Paar (Springer, Berlin, Heidelberg, 2003), p. 35.

[53] U. Rührmair, X. Xu, J. Sölter, A. Mahmoud, M. Majzoobi, F. Koushanfar, and W. Burleson, in *Cryptographic Hardware and Embedded Systems*, edited by L. Batina and M. Robshaw (Springer, Berlin, Heidelberg, 2014), p. 476.

[54] D. Le Sage, L. M. Pham, N. Bar-Gill, C. Belthangady, M. D. Lukin, A. Yacoby, and R. L. Walsworth, Efficient photon detection from color centers in a diamond optical waveguide, Phys. Rev. B **85**, 121202 (2012).

[55] C. A. Werley, M.-P. Chien, and A. E. Cohen, Ultrawide-field microscope for high-speed fluorescence imaging and targeted optogenetic stimulation, Biomed. Opt. Express **8**, 5794 (2017).

[56] A. M. Wojciechowski, M. Karadas, A. Huck, C. Osterkamp, S. Jankuhn, J. Meijer, F. Jelezko, and U. L. Andersen, Contributed review: Camera-limits for wide-field magnetic resonance imaging with a nitrogen-vacancy spin sensor, Rev. Sci. Instrum. **89**, 031501 (2018).

[57] A. M. Edmonds, Generation of nitrogen-vacancy ensembles in diamond for quantum sensors: Optimization and scalability of CVD processes, arXiv:2004.01746 (2020).